Rayleigh-Bénard-Marangoni Convection in an Open Cylindrical Container Heated by a Non-Uniform Flux

Rachid Es Sakhy, Kamal El Omari, Yves Le Guer, Serge Blancher

Rayleigh–Bénard–Marangoni convection in an open cylindrical container heated by a non-uniform flux

Rachid Es Sakhy, Kamal El Omari*, Yves Le Guer, Serge Blancher

Laboratoire des Sciences de l'Ingénieur Appliquées á la Mécanique et au génie Electrique (SIAME), Fédération IPRA-CNRS, Université de Pau et des Pays de l'Adour (UPPA), Bat. d'Alembert, Avenue Jules Ferry, 64075 Pau Cedex, France

The numerical work presented in this paper concerns the three-dimensional simulation of the natural convection in a liquid film contained in a cylindrical container with a bottom of solid substrate heated from below by a non-uniform heat flux. Both buoyancy and thermocapillarity are considered in addition to heat conduction within the solid substrate. The Navier–Stokes and energy equations are solved by a 3D finite volume method. Original morphologies of stationary convective cells (type and number) are observed. The flow patterns were found to depend on several studied dimensionless numbers, which are Rayleigh, Biot and Marangoni numbers, and on the ratio of the thermal conductivities of the solid substrate and the fluid.

1. Introduction

In the literature concerning convective instabilities within horizontal liquid layers, the destabilizing temperature gradient across the layer is often assumed to be directly controlled from the outside of the system, through the boundary conditions below and above the layer. The instability due to gravity and density variations is called Rayleigh–Bénard (RB) instability, while Bénard–Marangoni (BM) instability refers to the case where the surface tension variations are the driving force. Rayleigh–Bénard–Marangoni (RBM) instability refers to the case where both effects are coupled.

The Rayleigh–Bénard–Marangoni convection is now widely recognized for its practical importance due to its presence in a wide variety of processes. In the area of chemical engineering applications, one example is the flow inside distillation columns [1,2] for which the mass transfer across an interface is strongly influenced by surface tension effects. The role of surface tension is also important in silicon crystal growth by the float zone technique [3] and film coating processes [4]. RBM convection also plays an important role in the drying process by evaporation. Thus, many studies have been performed to understand the phenomena involved in this process, among them those of Chen et al. [5], Buffone et al. [6], Toussaint et al. [7], Touazi et al. [8] and Machrafi et al. [9].

Since the work of Nield [10] published in 1964, the theoretical limit (for an infinite layer) beyond which the thermally stratified state of a fluid is destabilized under the effect of a vertical temperature gradient is known in the case of coupled thermogravity and thermocapillarity effects. Several authors have developed experimental studies taking into account this coupling. For example, Koshmeider et al. [11] have shown the influence of the container geometry and the aspect ratio on the number of convective cells and their form. Schatz et al. [12] gave a review of experimental studies of instabilities in free-surface flows driven by thermocapillarity for both large- and small-aspect-ratio geometries. Pasquetti et al. [13] studied Bénard–Marangoni flows with predominant buoyancy effects in a cylindrical vessel of a high Prandtl number fluid. Rahal et al. [14] studied the influence of Biot, Prandtl, and Marangoni numbers on convection in small cylindrical containers.

To better understand the phenomena underlying these flows, other authors used numerical simulation. We cite, for example, the work of Béckle et al. [15] in which 2D simulations of combined buoyant and thermocapillary convection are compared to experimental results [16]. Kuhlmann et al. [17] simulated numerically the

* Corresponding author.
E-mail addresses: kamal.elomari@univ-pau.fr, kamal.elomari@gmail.com (K. El Omari).

Nomenclature

Bi	Biot number, $Bi = he/k_f$
d	thickness of the solid substrate, m
e	depth of the liquid layer, m
g	gravitational acceleration, m s^{-2}
h	heat transfer coefficient, W m^{-2} k^{-1}
k	thermal conductivity, W m^{-1} K^{-1}
K	conductivities ratio, $K = k_s/k_f$
Ma	Marangoni number, $Ma = \frac{e}{\mu\alpha}\frac{\Delta T}{\partial T}\frac{\partial\sigma}{\partial T}$
p	pressure, Pa
Pr	Prandtl number, $Pr = \nu/\alpha$
q	heat flux density, W m^{-2}
R	container radius, m
Ra	Rayleigh number, $Ra = g\beta\Delta Te^3/\nu\alpha$
t	time, s
T	temperature, K
V	velocity, m s^{-1}

Greek symbols

α	thermal diffusivity, m^2 s^{-1}
β	volumetric expansion coefficient, K^{-1}
ΔT	temperature difference, K
Γ	aspect ratio, $\Gamma = R/e$
μ	dynamical viscosity, kg m^{-1} s^{-1}
ν	kinematic viscosity, m^2 s^{-1}
ρ	density, kg m^{-3}
σ	surface tension, N m^{-1}
θ	reduced temperature, $\theta = (T-T_0)/\Delta T$

Subscripts

0	reference value
f	fluid
l	local value
m	mean value
s	solid
S/L	substrate/liquid interface

thermocapillary convection alone in systems of finite size, while Médale et al. [18] and Kuhlmann et al. [19] simulated both thermocapillary and buoyancy convection in small aspect-ratio containers. Several studies have been made in this context. For example, Kulhmann et al. [20] and Leypoldt et al. [21] modelled numerically the thermocapillary flows in two geometries, namely, a rectangular cavity and a cylindrical liquid bridge. The case of unsteady three-dimensional numerical simulation in an annular pool has also been addressed by Li et al. [22] and Hoyas et al. [23]. RBM convection is also very dependent on boundary conditions and geometry.

Other studies investigated how the system is heated, and we cite as an example the works of Koschmieder [24] and Rapier [25], who used a non-uniform heat flux at the cavity bottom. In contrast, Kuhlmann et al. [19] heated the liquid pool from above by a heat flux with a parabolic radial profile. Another way to apply a temperature gradient to a liquid film is to heat it through a solid substrate placed beneath it. Applying a non-uniform heating or using a substrate with a non-uniform thermal conductivity [26] both result in a non-uniform temperature profile at the substrate-liquid (S/L) interface. Furthermore, this profile is intimately related to the flow within the liquid, since they are closely dependent one another.

The RBM cellular flow patterns can be obtained for both cases of vertical or horizontal temperature gradients. The latter case can arise when the vertical walls of a cavity are differentially heated, while the former case can be obtained for a liquid cavity heated from below. In this case, thermocapillarity forces appear as soon as the temperature at the free surface has a non-uniform distribution. The particular case of thermocapillary convection driven by a horizontal temperature gradient was studied by several authors. Zebib et al. [27] and Ben Hadid et al. [28] presented numerical results concerning thermocapillary flows in cavities with different aspect ratios, while Mercier and Normand [29] and Peng et al. [30] performed numerical simulations for rectangular and annular pools, respectively. The features of two- and three-dimensional thermocapillary convection were investigated by Xu and Zebib [31]. A linear stability analysis was presented by Kuhlmann and Albensoeder [20] for the buoyant-thermocapillary flow in an open rectangular cavity with various aspect ratios: a stationary 3D cellular flow was obtained for a small aspect ratio, while, for large aspect ratio, hydrothermal waves appeared.

Frequently, both horizontal and vertical temperature gradients coexist, which makes RBM convection more complicated. Few studies have considered this combination of temperature gradients. To study the influence of the buoyancy effect on the formation of thermocapillary convective patterns under such a temperature gradient, a broad range of liquid layer thickness was considered by Ueno et al. [32] and Mizev and Schwabe [33].

Another difficulty in the study of BM convection or RBM convection is the consideration of possible deformation of the upper free surface, which was addressed by Cerisier et al. [34], El-Gamma et al. [35] and Bjøntegaard et al. [36].

In this paper, we present a numerical study of the RBM flow of a liquid film in a cylindrical container with a free upper surface, heated from below by a heat flux applied non-uniformly to a solid substrate forming the bottom of this container. This non-uniform heat flux leads to a combined action of a horizontal and vertical temperature gradient and to the formation of original flow patterns and convective cells.

First, we describe the physical configuration studied and the mathematical model (equations governing the flow with adequate boundary conditions) and assumptions used in the study. After a thorough mesh size dependence study, we present and discuss the obtained results for flows with a large range of parameters, such as Biot, Rayleigh or Marangoni numbers. The effect of the conjugated heat transfer through the conductive bottom is also discussed.

2. Physical and mathematical models

2.1. Basic assumptions and governing equations

We consider an incompressible Newtonian fluid layer of thickness e contained in an open cylindrical container of aspect ratio $\Gamma = R/e$. The side walls are assumed to be adiabatic, and a uniform heat flux q is imposed to the central part of the bottom of the solid substrate (Fig. 1). Heat conduction in this substrate creates an axisymmetric bell-shaped temperature distribution on the substrate/liquid interface (S/L). Buoyancy and thermocapillary forces give rise to convective cells whose shape depends on the geometry (aspect ratio) and the thermal conductivities ratio $K = k_s/k_f$.

The equations governing the flow are the mass, momentum and energy conservation equations. To address the conjugate heat transfer, the equations are solved over a computational domain covering both fluid and solid regions. In the solid zone, we prescribe a very high viscosity value to obtain a zero velocity field. This solution procedure ensures the conservation of heat flux at the

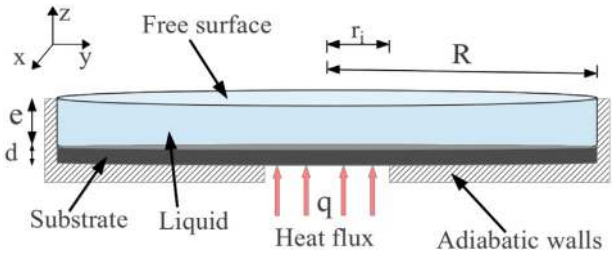

Fig. 1. Sketch of the physical system.

solid–liquid interface. For a simpler formulation of the problem, we consider a few approximations. We assume that the thickness of the fluid remains constant and the free surface is kept flat. The deformation of the free surface can be neglected if the Crispation number $Cr = \mu\alpha/\sigma e \ll 1$ and the Galileo number $Ga = ge^3/\nu\alpha \gg 1$ [8], which is the case for our study because $C_r = 5 \times 10^{-6}$ and $Ga = 3.7 \times 10^7$ for a typical flow configuration of our study (for example for a $e = 10$ mm layer of silicon oil with the following typical properties: $\mu = 2 \times 10^{-2}$ Pa s, $\nu = 2.1 \times 10^{-5}$ m^2/s, $\alpha = 10^{-7}$ m^2/s and $\sigma = 20 \times 10^{-3}$ N/m). The flow of RBM convection is due to the thermocapillary forces (an effect of the variation of surface tension with temperature) and buoyancy forces (an effect of the variation of density with temperature). It is assumed that the physical properties of the fluid are constant except for the surface tension (σ) and the density (ρ), which depend on the temperature. The fluid density variation is taken into account via the Boussinesq approximation. The following relations are considered:

$$\rho = \rho_0(1 - \beta(T - T_0)) \tag{1}$$

$$\sigma = \sigma_0\left(1 - \left.\frac{\partial\sigma}{\partial T}\right|_{T=T_0}(T - T_0)\right) \tag{2}$$

With the above assumptions, the flow and heat transfer equations are expressed in a non-dimensional form as follows:

$$\vec{\nabla}\cdot\vec{V} = 0 \tag{3}$$

$$\frac{\partial\vec{V}}{\partial t} + \vec{\nabla}\cdot(\vec{V}\otimes\vec{V}) = -\vec{\nabla}p + RaPr\ \theta\ \vec{z} + Pr\Delta\vec{V} \tag{4}$$

$$\frac{\partial\theta}{\partial t} + \vec{\nabla}\cdot(\vec{V}\theta) = \Delta\theta \tag{5}$$

The non-dimensional form of the equations results from scaling the lengths, velocities, time and temperature by the fluid layer thickness e, the thermal diffusion velocity α/e, the diffusion time e^2/α, and the temperature difference $\Delta T = qe/k_f$, respectively. The non-slip boundary condition is applied to the velocity at all the solid walls:

$$V_x = V_y = V_z = 0 \tag{6}$$

while the thermal boundary condition for the lateral adiabatic walls is

$$\left.\frac{\partial\theta}{\partial n}\right|_{r=\Gamma} = 0 \tag{7}$$

where n is the normal direction to the boundary. The thermal boundary condition at the solid–liquid interface is

$$K\left.\frac{\partial\theta}{\partial z}\right|_{z=0^-} = \left.\frac{\partial\theta}{\partial z}\right|_{z=0^+} \tag{8}$$

At the free surface ($z = 1$), the kinematic condition of mechanical equilibrium and the impermeability condition must be satisfied:

$$\frac{\partial V_x}{\partial z} + Ma\frac{\partial\theta}{\partial x} = 0 \tag{9}$$

$$\frac{\partial V_y}{\partial z} + Ma\frac{\partial\theta}{\partial y} = 0 \tag{10}$$

$$V_z = 0 \tag{11}$$

The thermal boundary condition at the free surface is a Robin condition:

$$\frac{\partial\theta}{\partial z} + Bi\ \theta = 0 \tag{12}$$

where $Bi = he/k_f$ is Biot number. h is the heat transfer coefficient between the free surface and the surrounding medium kept at a temperature T_0. The thermal condition at the central part substrate bottom is a prescribed heat flux of density q:

$$K\frac{\partial\theta}{\partial z} = 1 \quad \text{for} \quad z = -d/e = -1/4 \ \text{and}\ x^2 + y^2 \le (0.3\Gamma)^2 \tag{13}$$

The conservation equations (3)–(5) with their boundary conditions (6–13) were solved using an in-house parallel CFD code (Tamaris) developed in our laboratory (SIAME). This code has a three-dimensional unstructured finite-volume framework with hybrid meshes. More details about the numerical methods used here are given in Refs. [37–39]. Several validation studies of this code have been conducted in different flow situations and have been presented in previous authors' papers. Successful validations have been obtained for forced and natural convection [38,40,41], as well as for mixed and Marangoni convection [37].

All the computations were started from zero-velocity (rest) and isothermal ($T = T_0$) conditions.

2.2. Mesh size dependence study

The RBM flow is a highly non-linear phenomenon. The flow patterns that result for a predefined configuration are determined by a complex interaction between heat transport by convection, temperature gradients creation or destruction, surface thermocapillary forces and volume buoyancy forces. Thus, the numerical simulation of such flows requires a sufficiently fine mesh allowing a good resolution for the temperature gradients that are the driving force of Marangoni flows. To define the size of a mesh that gives a good compromise between accuracy and CPU cost, a study of the dependence of the computational results to the mesh size has been performed. The flow configuration used within this study corresponds to a flow in our studied geometry (Fig. 1) with $Ma = 2000$, $Ra = 1000$, $Bi = 100$ and $K = 100$. Five meshes with increasing size from 5×10^5 to 2×10^6 cells have been studied. All these meshes are refined at the boundaries, especially near the free surface. The relative error has been calculated by reference to the results given by the finest mesh. The compared quantities are the total kinetic energy E_C of the whole fluid volume Ω_f, computed as.

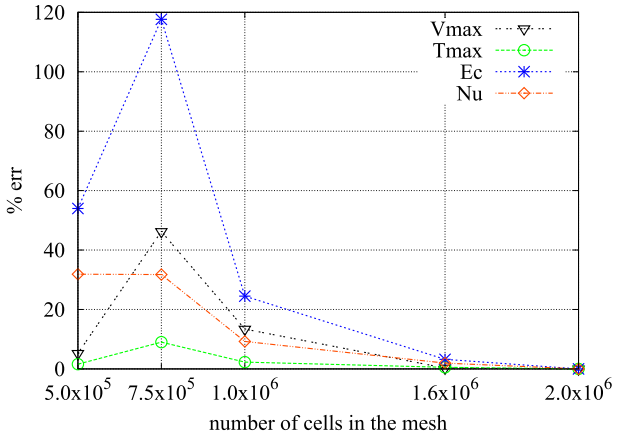

Fig. 2. The relative error of local (V_{max},T_{max}) and global (Nu, E_C) quantities vs. the mesh size.

$$E_C = \frac{1}{2\Omega_f} \int_{\Omega_f} (\vec{V} \cdot \vec{V}) \mathrm{d}v \tag{14}$$

The mean Nusselt number at the solid/liquid interface $S_{(S/L)}$ is computed using the following:

$$Nu_m = \frac{1}{S_{(S/L)}} \int_{S_{(S/L)}} Nu_l \ \mathrm{d}s \quad \text{at} \quad z = 0 \tag{15}$$

where Nu_l is the local Nusselt at this interface defined by

$$Nu_l = \frac{\vec{\nabla}\theta \cdot \vec{z}}{\theta}\Big|_{(S/L)} \quad \text{at} \quad z = 0 \tag{16}$$

Two other local extrema quantities are also used for this mesh size dependence study, which are the maximum velocity and the maximum temperature at the free surface ($z = 1$).

The relative error of these four quantities in reference to the results of the finer mesh are displayed in Fig. 2. We observe a substantial variation of most of these values for low size grids due to a change in the structure of the computed flow patterns. As can be seen in Figs. 3 and 9 convective cells has been captured by the 10^6 computational cells mesh, while only 8 cells has been captured by the 5×10^5 and 7.5×10^5 meshes. Again, 8 cells have been calculated by finer meshes (1.6×10^6 and 2×10^6). It is possible that the 9 convective cells pattern obtained by the 10^6 mesh would be a secondary solution of a flow situation presenting multiple solutions. However, it is likely to be a numerical artefact related to a non sufficiently refined mesh, since both of the finer meshes didn't detect this solution and that their results are quite similar. From these results, the crucial importance of the use of a sufficiently refined mesh is clearly highlighted, not only for the achievement of a good approximation of the global values but also for capturing all the features of the flow (convective cells). According to the results of this study, the chosen mesh for our study has been the mesh of 1.6×10^6 cells because the relative error for this mesh was found below 5% for all the monitored (local or global) quantities. (Fig. 4)

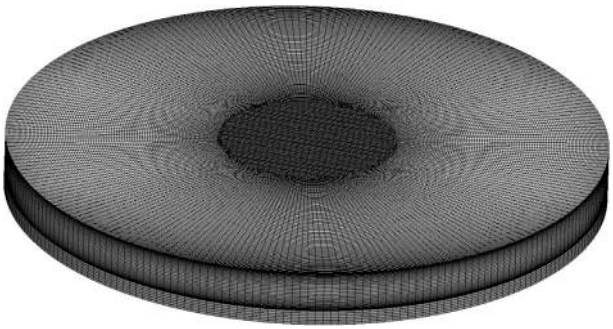

Fig. 4. The computational mesh used in the present study composed of 1.6×10^6 cells of hexahedral and prismatic shapes. Both the liquid and the solid substrate are meshed.

3. Results

As for the case of a uniformly heated fluid layer, the important flow parameters for the present case are the Ma, Ra, Bi and Pr numbers. Additionally, in our case, the ratio of the thermal conductivities $K = k_s/k_f$ is another relevant parameter. For this first work, we have restricted our study to the effect of the Biot, Rayleigh, Marangoni and ratio of thermal conductivities non-dimensional parameters. The effect of the Prandtl number is not included in the present paper as well as the one of the aspect ratio parameter Γ. They were fixed to Pr = 100 and $\Gamma = 5$. Unless specifically indicated, all the studied flow situations are steady. Thus, the results have been searched using a steady solver. The convergence was declared reached when the RMS of the residuals was below 10^{-6} for velocity, temperature and pressure. Nevertheless, the steady character of the flow has been verified for some particular situations by conducting unsteady computations to ensure that they give results identical to those of steady computation and that they do not evolve in time. These particular cases were those that showed a low convergence rate. Other particular cases were found to be unsteady flows, which will be indicated in the results, even if the present study focuses on steady situations.

3.1. Effect of the Biot number

In this first section we investigate the impact of the free surface cooling on the fluid flow and on the heat transfer at the solid surface. Thus, the Bi number has been varied while the other

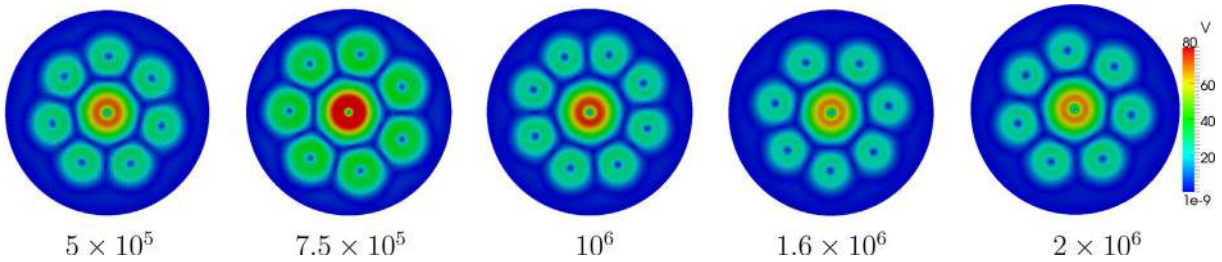

Fig. 3. Velocity field at the free surface of the liquid for different mesh sizes [Ma = 2000, Ra = 1000, Bi = 100, Pr = 100 et $K = 100$].

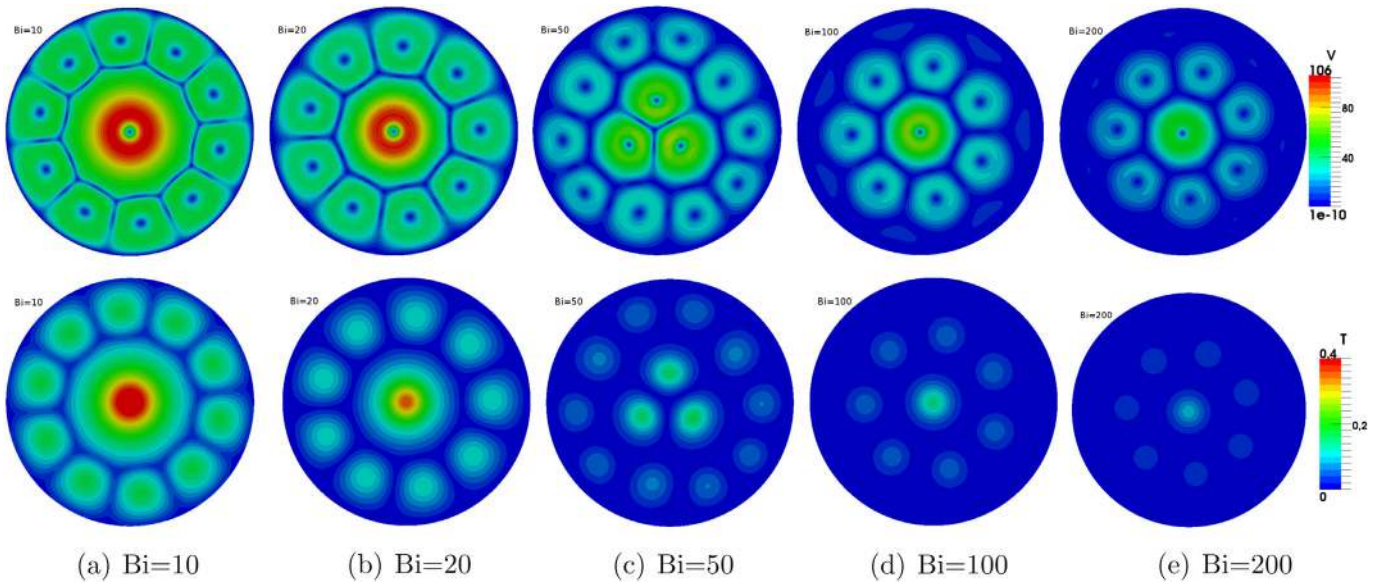

Fig. 5. Velocity (top) and temperature (bottom) fields at the free surface for different Biot numbers [Ma = 2000, Ra = 1000, Pr = 100 and $K = 100$].

parameters have been kept constant ($Ma = 2000$, $Ra = 1000$, $Pr = 100$ and $K = 100$).

Fig. 5 shows the velocity and temperature distribution at the free surface of the liquid for different Biot numbers. For the lowest Bi value studied ($Bi = 10$), we obtain a large convective cell at the center of the container surrounded by 10 peripheral cells. When the heat exchange at the free surface is increased by increasing the Bi number, the size and the number of the cells decrease progressively to reach 7 cells for $Bi = 200$, while the overall intensity of the velocity becomes weaker. At approximately $Bi = 50$, the large central toroidal fluid recirculation breaks into three weaker convective cells. The augmentation of the heat exchange (i.e., of the Bi) results in a decrease of the temperature level at the free surface (Fig. 5). However, the decrease of the velocity observed in the same figure is

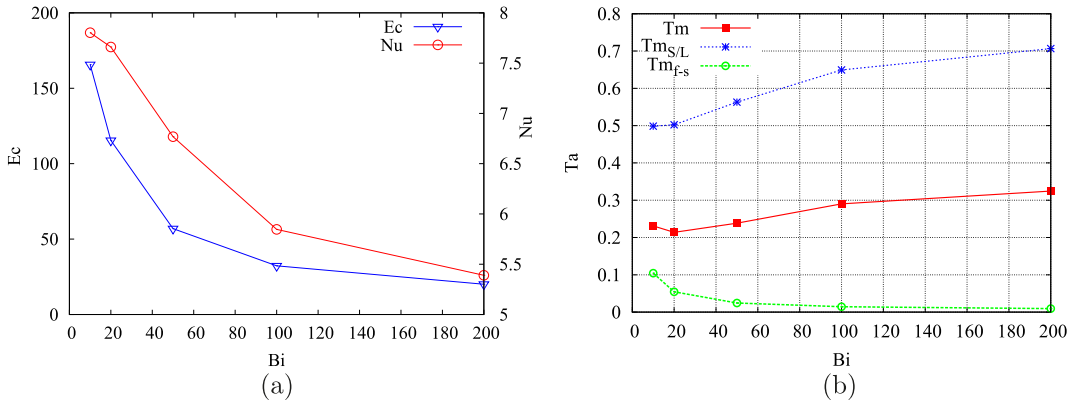

Fig. 6. (a) Kinetic energy of the fluid and average Nusselt number, (b) averaged temperatures of the fluid (T_m), the solid–liquid interface ($T_{m_{S/L}}$) and of the free surface ($T_{m_{fs}}$), for different Biot numbers [Ma = 2000, Ra = 1000, Pr = 100 and $K = 100$].

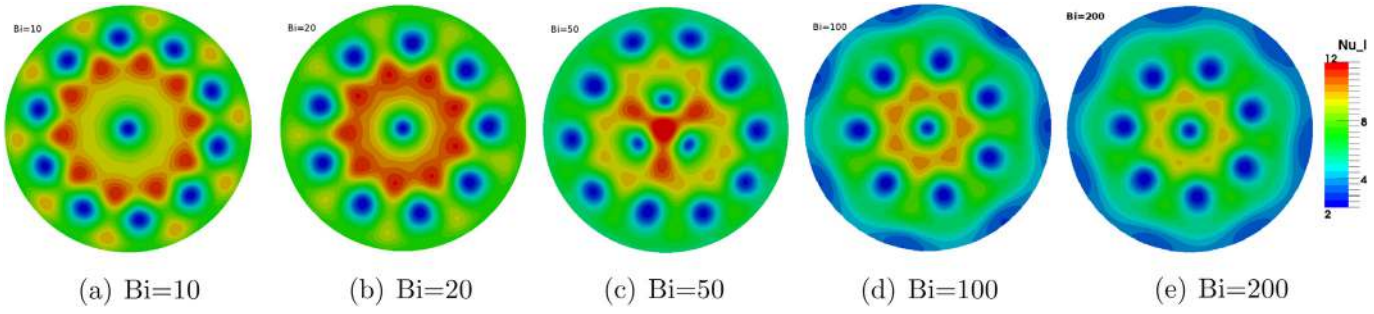

Fig. 7. Local Nusselt number (Nu_l) for different Biot numbers at the substrate-liquid interface [Ma = 2000, Ra = 1000, Pr = 100 et $K = 100$].

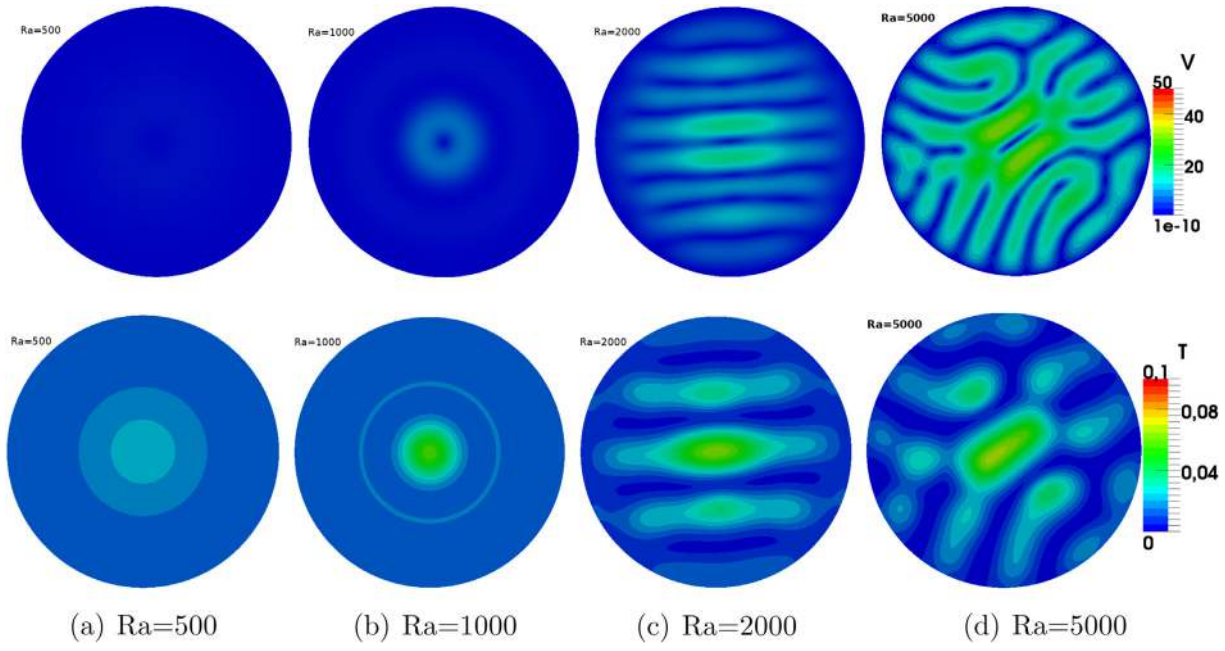

Fig. 8. Velocity (top) and temperature (bottom) fields at the free surface for different Rayleigh numbers [Ma = 0, Bi = 100, Pr = 100 and $K = 100$].

explained by a global decrease of the temperature tangential (horizontal) gradients at the free surface.

These observations agree with the linear stability analysis results of Nield [10] and Pearson [42] where they showed that increasing the heat transfer at the free surface stabilizes the flow. Thus higher capillary forces are needed to trigger the flow which corresponds to a higher critical Marangoni. Similar observations were made by Touihri et al. [43] in the case of an open cylindrical container heated uniformly from below. They showed that when capillary and buoyancy forces act in the same direction, a higher critical Ra_c number is needed to destabilize the flow when the Bi is increased for a fixed Ma.

The overall diminution of the fluid agitation is clearly shown in Fig. 6(a), which gives the variation of the globally averaged kinetic energy E_C as computed by Eq. (14) and that shows a steep decrease of E_C for low Bi values, followed by a stabilization for $Bi > 100$. Indeed, with the Biot increase, the thermal boundary condition at the free surface tends towards an imposed and uniform temperature condition, what suppresses gradually the Marangoni convection and weakens the heat transfer from the bottom plate as shown in Fig. 6(a) that gives the global heat transfer at the substrate-liquid interface quantified by the average Nusselt number (Eq. (15)) and which shows a strong decrease with the augmentation of the Biot number. The evolution of the Nusselt number with the Biot number follows relatively well the evolution of the kinetic energy (on the same figure). Again, we can explain the decrease of heat transfer at the bottom of the pool by the decrease of the fluid motion when higher cooling is applied at the free surface. In Fig. 6(b), the

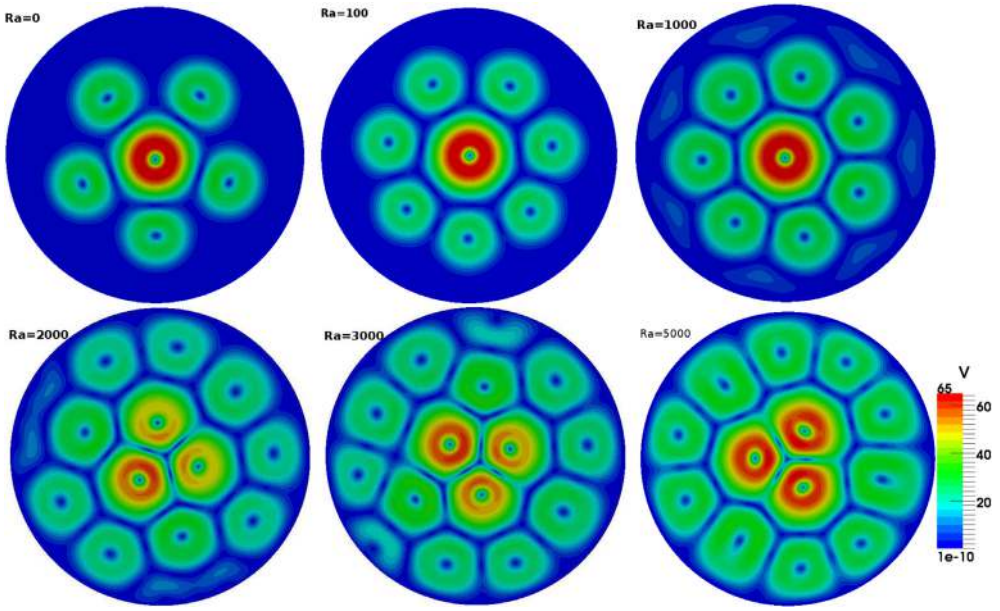

Fig. 9. Velocity at the free surface for different Rayleigh numbers [Ma = 2000, Bi = 100, Pr = 100 and K = 100].

examination of the average temperatures of the fluid T_m and of the fluid–solid interface (the pool bottom) $T_{m_{S/L}}$, shows an increase with the increase of the Bi number, while the free surface temperature $T_{m_{fs}}$ decreases. The augmentation of T_m and $T_{m_{S/L}}$ is due to a less efficient heat transport by convection within the fluid layer as a result of the weakening of the thermocapillary forces and fluid velocity. Thus, for such a thermocapillary-driven flow with a moderate Rayleigh number ($Ra = 10^3$), enhancing the heat transfer at the free surface worsens the heat transfer at fluid–solid interface. Since a fixed heat flux is imposed at the bottom of the pool as a thermal boundary condition, the same heat flux rate needs to be transferred through the liquid layer when the Bi is changed. Thus, when the heat transfer coefficient is increased at the free surface (higher Bi), the temperature at this surface ($T_{m_{fs}}$) approaches the surrounding temperature T_0. In a purely conductive layer, such a decrease of $T_{m_{fs}}$ comes along by a decrease of the bottom temperature $T_{m_{S/L}}$ to preserve the same heat flux rate. In the case of a convective liquid layer (our case), we observe, contrarily to the conductive case, an increase of $T_{m_{S/L}}$. This is due to the above-mentioned weakening of the convection within the liquid layer. We can give a global picture of this behaviour by considering h_c to be a global convective heat transfer coefficient between the bottom of the liquid and its free surface, while h being the coefficient at the free surface. The conservation of the heat flux q writes:

$$q = h\left(T_{m_{fs}} - T_0\right) = h_c\left(T_{m_{S/L}} - T_{m_{fs}}\right)$$

thus:

$$T_{m_{S/L}} = T_{m_{fs}} + \frac{q}{h_c} = T_0 + \frac{q}{h} + \frac{q}{h_c}$$

From the latter expression we can conclude that the effect of the decrease of h_c (convection in the liquid) is stronger than the effect of increase of h (i.e. of Bi), since $T_{m_{S/L}}$ increases.

The distribution of heat transfer at the solid–liquid interface is examined in Fig. 7 by plotting the distribution of the local Nusselt (Eq. (16)) for different Bi numbers. In this figure, we see that the Nu_l distribution shows different patterns with Bi variation. High Nu_l value spots correspond to zones where the fluid is descending from the free surface at lower temperature, while low Nu_l value spots correspond to zones of ascending hot fluid. For $Bi = 10$, we can observe the formation of numerous high Nu_l spots including in the regions near the lateral walls. For $Bi = 200$, few of these spots are present and lower Nu_l value spots are larger and cover the entire peripheral region. For the case of $Bi = 50$, the presence of three convection cells at the pool center results in the highest observed Nu_l value ($Nu_l \approx 13$), located at the center of the container. For all other values of Bi, Nu_l reach its lowest value ($Nu_l \approx 2$) at this position (and at the cell centers).

3.2. Effect of buoyancy (Rayleigh number)

Prior to studying the coupled effects of thermocapillarity and buoyancy, we will analyse the flow features in the absence of the Marangoni effect. This preliminary study will allow us to better understand the effect of thermocapillarity on the flow. In the following sections, the value of the Biot number is fixed to a value of 100. It is a rather high value, corresponding to a conceptual specific situation were the temperature of the surrounding medium is almost imposed uniformly at the free surface of the liquid. Such a situation can be approached inside a specific device containing for example a liquid layer of $e = 10$ mm thickness and whose conductivity is equal to $k_f = 0.1$ W/m K, covered by a fine layer of helium ($e_h = 150$ μm and $k_h \approx 0.15$ W/m K). Thus, considering the sole thermal conduction through the gas layer (neglecting radiation), the Biot number would be $Bi = (e/e_h)\cdot(k_h/k_f) = 100$.

3.2.1. Absence of thermocapillarity at the free surface

In this section, the Marangoni number is set to zero ($Ma = 0$) and Ra is varied from $Ra = 500$ to 5000. Fig. 8 shows the velocity and the temperature of the fluid at the free surface. For the low Ra value (500), the fluid is almost at rest while the temperature at the center of the surface is slightly above the reference temperature (T_0), which is mainly due to thermal conduction in the fluid. In this case, very weak but non-zero velocities are observed. On the contrary to the classical Rayleigh–Bénard flow, for which the critical value of Ra is 1707.76 [44], no such a threshold holds for our case, and this is due to the presence in the fluid of a horizontal component of the temperature gradient, consequence of the non-uniform heating [45].

For $Ra = 1000$, a weak convection cell forms at the container center and the temperature field at the free surface suggests the presence of a second weaker toroidal cell around the central one. These dissipative structures have been experimentally highlighted for the first time by Koschmieder [46]. For $Ra = 2000$, parallel elongated rolls are formed (stripes). When Ra is fixed to 5000, this roll structure is destabilized and the flow is organized in fingering patterns and becomes unsteady. The flow in this case has no plan of symmetry, and the temperature and velocity fields showed in Fig. 8 are instantaneous ones and their patterns are similar to those observed experimentally and discussed by Croquette et al. [47]. They identified them as crossing and competitive sets of rolls. The multiplication of these sets of rolls attempts to release more thermal energy from the liquid as Ra is increased.

3.2.2. Buoyancy and thermocapillarity coupled effects

Fig. 9 shows the flow patterns for various Ra values in the case of significant thermocapillary forces. Thus, the Marangoni number was fixed at a rather high value, $Ma = 2000$ (the relative importance of this value will be discussed in Section 3.3).

The particular case of zero gravity has also been considered ($Ra = 0$). The thermocapillarity is clearly the effect responsible for the formation of the cellular flow patterns because this pure Marangoni flow situation presents five convective cells regularly distributed around a central cell (no concentric rolls observed here). The velocity field shows that this latter cell has a pentagonal shape, and the whole pattern has 5 planes of symmetry. The superposition of the buoyancy effect for $Ra = 100$, gives rise to two supplementary peripheral convection cells. The flow pattern now has 7 planes of symmetry. This very low Ra value, which does not trigger the flow in the case of $Ma = 0$ (Fig. 8), significantly changes the flow structure when $Ma = 2000$. The interaction between Marangoni and buoyancy forces is observed even when the latter forces are weak. Thus, when the convection is triggered by thermocapillarity, a weak buoyancy can play a significant role.

From $Ra = 100$ to 1000, the number of convective cells does not change, whereas their size increases. At $Ra = 2000$, the central cell is replaced by 3 cells with lower velocity level. A number of 12 convective cells are now present in the container and the flow pattern has only one plane of symmetry. The central cells become now of hexagonal shape and the peripheral ones are of irregular shape due to the confinement imposed by the circular geometry of the boundary. For $Ra = 3000$, we observe the birth of a new cell and two incomplete ones due to the effects of the lateral boundary. For $Ra = 5000$, these incomplete cells merge with other neighbouring cells and the flow shows 13 large well defined convective cells (3 central and 10 peripheral). Again, for $Ra = 3000$ and 5000, only one plane of symmetry is present. The hexagonal shape of the cells is

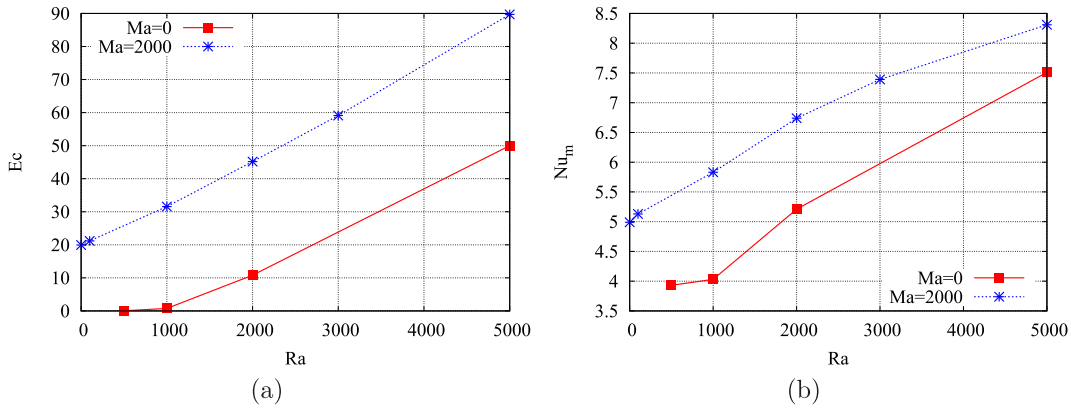

Fig. 10. (a) Kinetic energy of the fluid, and (b) average Nusselt number for various Rayleigh numbers and two Ma values [Bi = 100, Pr = 100 and $K = 100$].

the dominating structure when the velocities at the surface are high (i.e. in the central part of the container).

The continuous birth and reorganization of new convective cells is a consequence of the augmentation of the kinetic energy in the fluid with the increase of *Ra* number. This augmentation is shown in Fig. 10(a) for both $Ma = 0$ and $Ma = 2000$. The evolution of *Ec* vs. *Ra* is almost linear with a slightly higher slope for $Ma = 2000$. As expected, *Ec* values are higher for $Ma = 2000$, since stronger capillary forces are involved. Again the evolution of the Nusselt number, given in 10(b), follows roughly the evolution of E_C, since it is a consequence of the fluid agitation, particularly in the vicinity of the bottom plate. For stationary patterns, the continuous generation of kinetic energy results from an equilibrium between continuous release of potential energy due to the localized heating at the bottom plate and the cooling at the free surface and the viscous dissipation within the fluid.

3.3. *Effect of thermocapillarity (Marangoni number)*

In this section, we analyse the effect of the Marangoni number on flow and heat transfer. To vary the *Ma* number of the flow, we modify the value of the quantity $\partial\sigma/\partial T|_{T=T_0}$, while the values of the other parameters remain unchanged ($Ra = 1000$, $Bi = 100$, $Pr = 100$ and $K = 100$).

In Fig. 11, we show the velocity fields obtained for *Ma* values ranging from 500 to 2500. The flow situation of $Ma = 0$ can be found in Fig. 8 ($Ra = 1000$). For the lowest studied value $Ma = 500$, we can see that the Marangoni effect is responsible for the formation of 6 peripheral convective cells around a central hexagonal cell. However, the velocity of the fluid is relatively weak. From $Ma = 1000$ to $Ma = 2000$, there are 7 peripheral cells with growing velocity as the *Ma* increases, and their sizes also increase. At $Ma = 2500$, the higher thermocapillary forces are responsible for the subdivision of the central cell into 3 cells and the appearance of 3 more peripheral cells. The cells fill now completely the container. The pattern observed is quite similar to the one observed for $Ra = 5000$ and $Ma = 2000$ in Fig. 9. For this *Ma* value, only one plane of symmetry is clearly identified for the pattern of the flow. In all these flow situations, the central cell exhibits higher values of both velocity and temperature (Fig. 11) at the fluid surface than those exhibited by peripheral cells: $\simeq \times 3$ for temperature and $\simeq \times 2$ for velocity. This is due to the combined effect of the centred heating and the constraint imposed by the lateral circular wall.

As for Ra number, the augmentation of *Ma* results in a significant increase in the kinetic energy of the fluid (Fig. 12 (a)). This

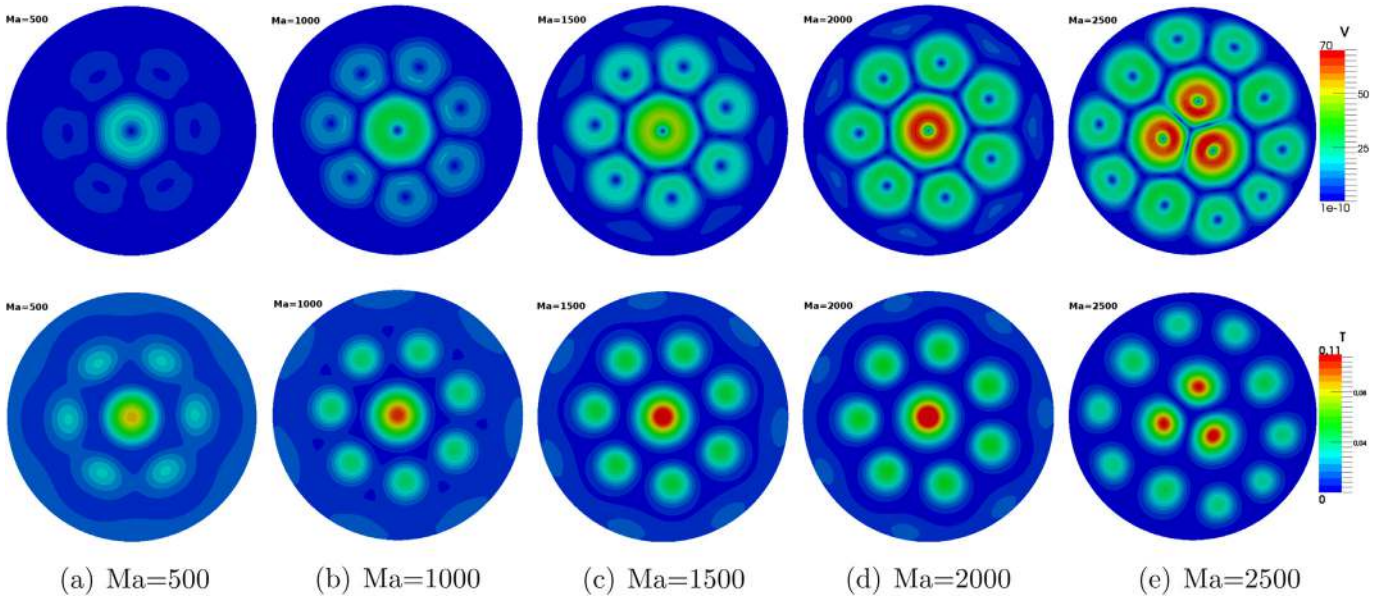

Fig. 11. Velocity (top) and temperature (bottom) fields at the free surface for different Marangoni numbers [Ra = 1000, Bi = 100, Pr = 100 and $K = 100$].

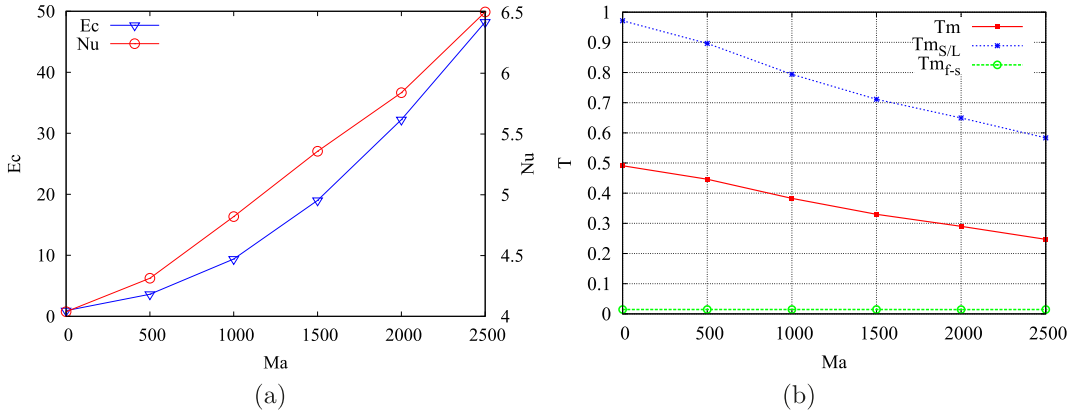

Fig. 12. (a) Kinetic energy and Nusselt number and (b) averaged temperatures of the fluid (T_m), the solid−liquid interface ($T_{m_{S/L}}$) and the free surface ($T_{m_{fs}}$), for different Marangoni numbers [Ra = 1000, Bi = 100, Pr = 100 and K = 100].

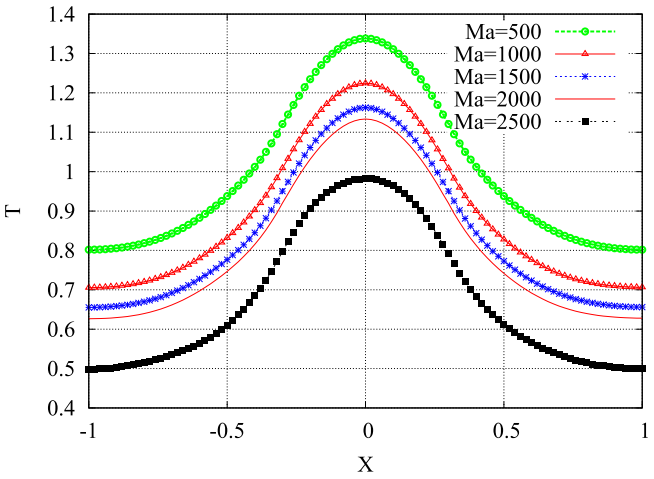

Fig. 13. Temperature at the substrate-liquid interface along the x-axis for different Ma values [Ra = 1000, Bi = 100, Pr = 100 and K = 100].

augmentation of the fluid agitation induces a diminution of the mean temperature of the fluid and the substrate-liquid interface, as seen in Fig. 12(b). The temperature of the free surface does not evolve with the increase of Ma because of the high value of the Biot number. The distribution of the temperature over this lower surface of the pool is axisymmetric and has a bell shape for the thermal conduction ratio studied here (K = 100). Fig. 13 shows this distribution along an axis of the liquid−solid interface. We can see in this figure that when the *Ma* value increases, the temperature curve translates downwards while keeping almost the same shape. The temperature profile is slightly spread for the case Ma = 2500. The notable modifications of the flow patterns related to the change of the Marangoni number observed in Fig. 11 do not affect the form of the temperature profile at this interface, but only its level. However, the downward shifting of the temperature profile does not vary linearly with Ma: it is more important between Ma = 500 and Ma = 1000 when the cells appear and also between Ma = 2000 and Ma = 2500 when the pattern of cells completely filled the container, indicating a better heat transfer towards the fluid in these cases. The general trend is that the global parietal heat transfer increases with the strengthening of the thermocapillarity forces and kinetic energy, as showed by Fig. 12(a).

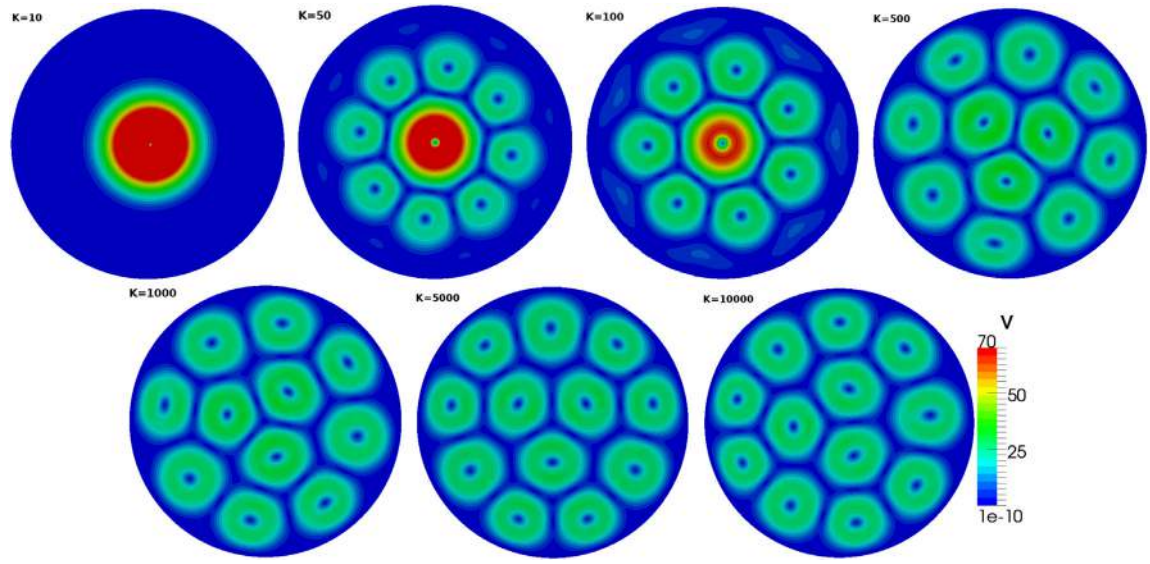

Fig. 14. Velocity at the free surface for different conductivity ratios K and for Ra = 1000 [Ma = 2000, Bi = 100 and Pr = 100].

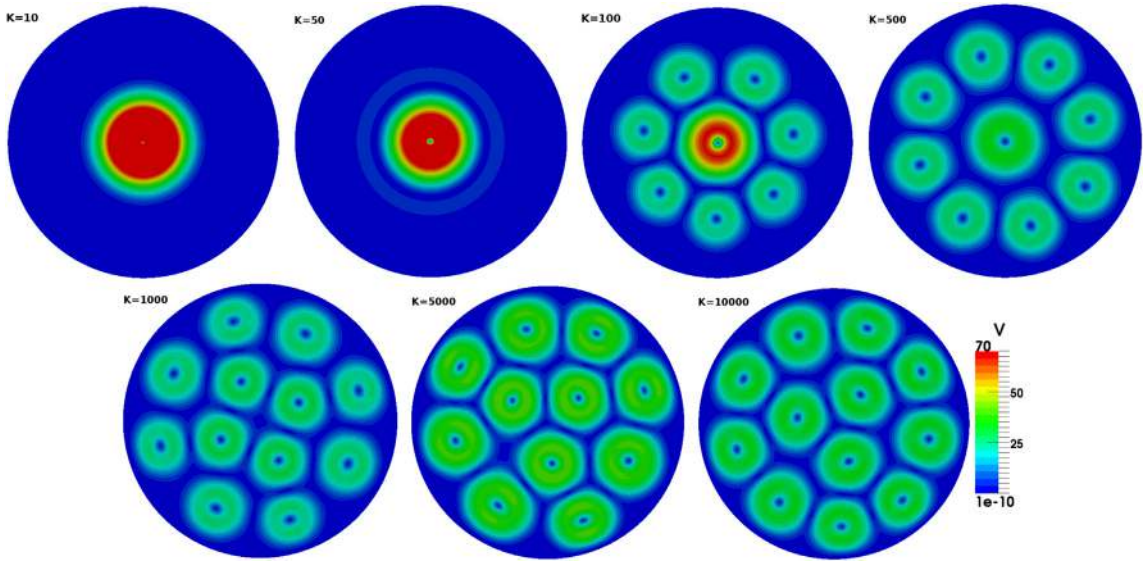

Fig. 15. Velocity at the free surface for different conductivity ratios K and for $Ra = 100$ [Ma = 2000, Bi = 100 and Pr = 100].

3.4. Influence of the thermal conductivities ratio K

The presence of thermally conductive walls is known to affect the temperature distribution at the boundaries of a studied system. It was frequently observed that some of the discrepancies that arise between the experimental and numerical simulation results are due to the heat transfer by conduction along the walls during experimentation [26,48]. Therefore, by taking into account the conjugated heat transfer in the flow simulation, the obtained numerical results are found to be in better agreement with experimental observation and measures [49]. In this section, we investigate the role played by the solid substrate at the bottom of the container. Indeed, the difference between the thermal conductivities of the fluid and the solid substrate determines the temperature distribution at the container bottom and changes the flow patterns. Different values of the ratio $K = k_s/k_l$, ranging from 10 to 10^4 (i.e. low to very high thermal conductivity substrate for the same fluid), have been studied. According to the value of K, the heat flux boundary condition applied at the center of the bottom of the substrate will be perceived differently at the solid−liquid interface (the more K is high, the more the heat will be transferred radially within the substrate).

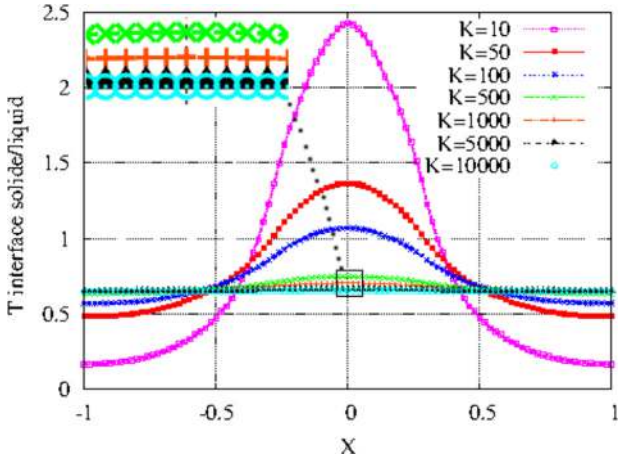

Fig. 16. S/L interface temperature along the x-axis for different conductivity ratios K. Top left inset: a zoom of the area around $r = 0$ [Ma = 2000, Bi = 100, Pr = 100 and Ra = 1000].

In Figs. 14 and 15, we present the velocity distribution, at the free surface for two different Rayleigh numbers, $Ra = 1000$ and $Ra = 100$, respectively, and for different values of K. For the case of $Ra = 1000$ (Fig. 14), significant changes in the flows patterns are observed for $10 < K < 5000$, and above approximately $K = 5000$, no substantial differences are observed. Thus, for $K = 10$, only a large convective cell is observed, located at the container center. This behaviour is due to a temperature distribution at the S/L interface exhibiting a high centered peak, as seen in Fig. 16, while the peripheral zone is relatively cold. At a higher value ($K = 50$, Fig. 14), eight peripheral cells appear. The peak of the temperature distribution at the fluid bottom is shorter (Fig. 16). For $K = 100$, seven large peripheral cells are visible, while for $K = 500$, a new flow configuration takes place in the container with three central convective cells, and the flow pattern fills all the extent of the container. This configuration changes slightly for higher values of K (500, 1000, 5000, 10^4), with the formation of an additional peripheral cell between $K = 1000$ and $K = 5000$, because the temperature distribution at the fluid bottom for these K values is almost flat (Fig. 16). Thus, beyond $K > 5000$, increasing the thermal conductivity of the solid substrate does not significantly change the temperature distribution at the S/L interface, and, as a consequence, the flow pattern remains unchanged. These types of flow patterns obtained for high K values are similar to some of those obtained experimentally by Rahal et al. [14] in a cylindrical container with an aspect ratio $\Gamma = 6$, uniformly heated from below but for different values of flow parameters.

For a rather small Rayleigh number ($Ra = 100$), the thermocapillary force is the only force responsible for the formation of the flow patterns. Thus, for $K = 10$ and $K = 50$ (Fig. 15), only a large convective cell is observed in the container center. Beyond $K \approx 100$, peripheral cells appear, but, for each conductivity ratio K, the cells organization is different. Seven peripheral cells are found around a central one for $K = 100$, and one more peripheral cell is found for $K = 500$. From $K = 500$, the cell pattern fills the overall surface of the container. The fact that flow patterns do not fill the container for $K < 500$ is caused by the combination of a rather high Bi at the free surface and of a centred temperature profile at bottom. New

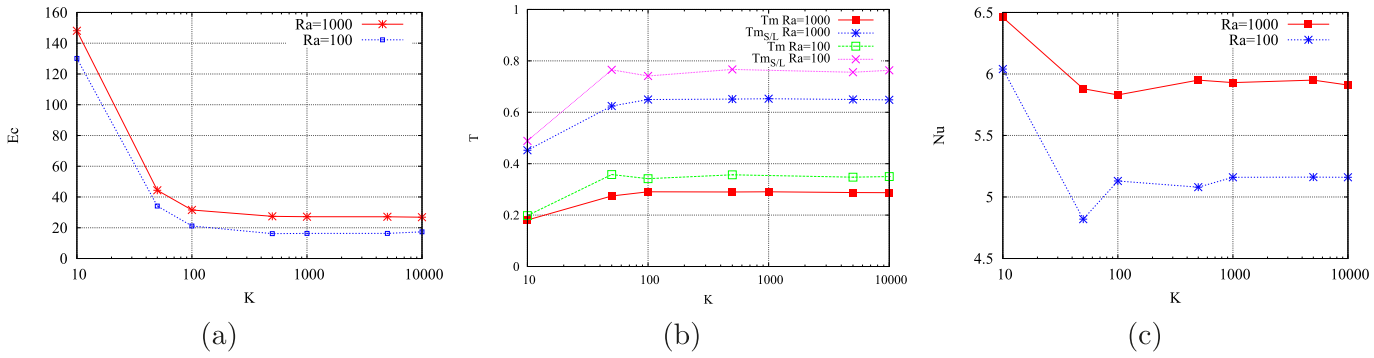

Fig. 17. Kinetic energy of the fluid (a), averaged temperatures T_m and $T_{m_{S/L}}$ (b) and average Nusselt number (c) for various conductivity ratios K and for two Ra values (100 and 1000) [Ma = 2000, Bi = 100 and Pr = 100].

flow configurations are observed for the final three conductivity ratios ($K = 1000$, $K = 5000$ and $K = 10^4$): the central cell is replaced by four cells in the center for $K = 1000$, while for $K = 5000$, one central cell disappears and one peripheral cell appears. For $K = 10^4$, an additional peripheral cell forms. From this study, we can conclude that the effect of buoyancy forces on the flow patterns is more significant for low and moderate values of K, since strong buoyancy ascendant fluid currents form above the central hot spot of the substrate. However, for global quantities, the effect of K is not noticeable beyond $K \approx 100$, which corresponds to the formation of cellular flow pattern for both Ra values, as we can see in Fig. 17. The volume averaged kinetic energy Ec and fluid temperature, as well as the surface averaged Nu and S/L interface temperature, exhibit almost unchanged values for $K > 100$. For $K = 10$, the kinetic energy reaches a rather high value related to a strong convection in the narrow zone above the hot spot that forms at the substrate center, while the remaining fluid in almost at rest. For higher K values, even if a large number of additional convective cells form, the kinetic energy of the fluid is approximately 5 times lower than for $K = 10$. We recall that Ma, Ra and Bi are kept unchanged. In the previous sections of this study, when these parameters were varied, the formation of new flow structures or convective cells always goes along with an increase in E_C. When varying K, the spread over the substrate of the supplied heat flux to the fluid, creates multiple convective cells of moderate velocities whose global kinetic energy is lower than that generated by the concentrated heat flux injection.

4. Conclusion

A series of 3D numerical simulations of thermocapillary-buoyancy convection in an open container, heated from below by a non-uniform heat flux, were achieved using the finite volume method and taking into account the presence of a conductive bottom. From the obtained results, the following conclusions can be formulated:

- The flow structure is affected by thermocapillary effects acting on the free surface and by the buoyancy effect. However, the regular convective cells are mainly due to the thermocapillarity effect. Nevertheless, even weak buoyancy noticeably affects the flow patterns generated by thermocapillarity.
- The flow depends on the substrate to fluid conductivity ratio. Thus, for small conductivity ratios, the temperature profile at the container bottom forms a narrow peak and only one cell is observed in the container center. For larger conductivity ratios, the peripheral convective cells appear, due to a flat parietal temperature profile.
- The heat exchange at the free surface (Bi) has a significant effect on the flow patterns, specifically for low or moderate Biot numbers for which the kinetic energy of the fluid is high because of the non uniform temperature distribution at the free surface, that causes high thermocapillary forces. Thus a high Bi results in a weak Marangoni convection and a global augmentation of the liquid temperature.
- All these effects appear as changes in the number of convective cells and their distribution in the container. The augmentation of the kinetic energy E_C always manifests itself by an increase of the number and extent of the convective cells, except for the case of the augmentation of the conductivities ratio, for which E_C is lower when more convective cells are observed (for flat temperature profiles at the bottom).

Acknowledgements

This work received the support of the PHC of Volubilis Morocco-France (Integrated Action N. MA/09/214-Morocco MA/09/213-France) and the authors were granted access to the HPC resources of CINES under the allocation 2012-c2012026738 made by GENCI (Grand Equipment National de Calcul Intensif).

References

[1] F. Zuiderweg, A. Harmens, The influence of surface phenomena on the performance of distillation columns, Chem. Eng. Sci. 9 (2–3) (1958) 89–103.
[2] W.B. Patberg, A. Koers, W.D.E. Steenge, A.A.H. Drinkenburg, Effectiveness of mass transfer in a packed distillation column in relation to surface tension gradients, Chem. Eng. Sci. 38 (6) (1983) 917–923.
[3] Y. Shen, G. Neitzel, D. Jankowski, H. Mittelmann, Energy stability of thermocapillary convection in a model of the float-zone crystal-growth process, J. Fluid Mech. 217 (1) (1990) 639–660.
[4] P. Calvert, Inkjet printing for materials and devices, Chem. Mater. 13 (10) (2001) 3299–3305.
[5] J.J. Chen, J.D. Lin, Thermocapillary effect on drying of a polymer solution under non-uniform radiant heating, Int. J. Heat. Mass Transf. 43 (12) (2000) 2155–2175.
[6] C. Buffone, K. Sefiane, W. Easson, Marangoni-driven instabilities of an evaporating liquid-vapor interface, Phys. Rev. E 71 (5) (2005) 056302.
[7] G. Toussaint, H. Bodiguel, F. Doumenc, B. Guerrier, C. Allain, Experimental characterization of buoyancy-and surface tension-driven convection during the drying of a polymer solution, Int. J. Heat. Mass Transf. 51 (17) (2008) 4228–4237.
[8] O. Touazi, E. Chénier, F. Doumenc, B. Guerrier, Simulation of transient Rayleigh-Bénard-Marangoni convection induced by evaporation, Int. J. Heat. Mass Transf. 53 (4) (2010) 656–664.
[9] H. Machrafi, A. Rednikov, P. Colinet, P.C. Dauby, Bénard instabilities in a binary-liquid layer evaporating into an inert gas, J. Colloid Interface Sci. 349 (1) (2010) 331–353.
[10] D. Nield, Surface tension and buoyancy effects in cellular convection, J. Fluid Mech. 19 (3) (1964) 341–352.
[11] E.L. Koshmeider, S.A. Prahl, Surface-tension-driven Bénard convection in small containers, J. Fluid Mech. 215 (1990) 571–583.

[12] M.F. Schatz, G.P. Neitzel, Experiments on thermocapillary instabilities, Annu. Rev. Fluid Mech. 33 (1) (2001) 93–127.
[13] R. Pasquetti, P. Cerisier, C. Le Niliot, Laboratory and numerical investigations on Bénard–Marangoni convection in circular vessels, Phys. Fluids 14 (2002) 277.
[14] S. Rahal, P. Cerisier, H. Azuma, Bénard–Marangoni convection in a small circular container: influence of the Biot and Prandtl numbers on pattern dynamics and free surface deformation, Exp. Fluids 43 (4) (2007) 547–554.
[15] U. Bückle, M. Perić, Numerical simulation of buoyant and thermocapillary convection in a square cavity, Numer. Heat. Transf. 21 (2) (1992) 121–141.
[16] H.C. Kuhlmann, Thermocapillary flows in finite size systems, Math. Comput. Model. 20 (10–11) (1994) 145–173.
[17] V. Sa, H.C. Kuhlmann, H. Rath, Investigation of three-dimensional thermocapillary convection in a cubic container by a multi-grid method, Int. J. Heat. Mass Transf. 39 (3) (1996) 603–613.
[18] M. Médale, P. Cerisier, Numerical simulation of Bénard–Marangoni convection in small aspect ratio containers, Numer. Heat. Transf. A Appl. 42 (1) (2002) 55–72.
[19] H.C. Kuhlmann, U. Schoisswohl, Flow instabilities in thermocapillary-buoyant liquid pools, J. Fluid Mech. 644 (2010) 509–535.
[20] H.C. Kuhlmann, S. Albensoeder, Three-dimensional flow instabilities in a thermocapillary-driven cavity, Phys. Rev. E 77 (3) (2008) 36303.
[21] J. Leypoldt, H.C. Kuhlmann, H.J. Rath, Three-dimensional numerical simulation of thermocapillary flows in cylindrical liquid bridges, J. Fluid Mech. 414 (2000) 285–314.
[22] Y.R. Li, L. Peng, Y. Akiyama, N. Imaishi, Three-dimensional numerical simulation of thermocapillary flow of moderate prandtl number fluid in an annular pool, J. Cryst. Growth 259 (4) (2003) 374–387.
[23] S. Hoyas, A.M. Mancho, H. Herrero, N. Garnier, A. Chiffaudel, Bénard–Marangoni convection in a differentially heated cylindrical cavity, Phys. Fluids 17 (2005) 054104.
[24] E.L. Koschmieder, Convection on a non-uniformly heated, rotating plane, J. Fluid Mech. 33 (3) (1968) 515–527.
[25] A.C. Rapier, Forced convection heat transfer in a circular tube with non-uniform heat flux around the circumference, Int. J. Heat. Mass Transf. 15 (3) (1972) 527–537.
[26] T. Gambaryan-Roisman, Marangoni convection, evaporation and interface deformation in liquid films on heated substrates with non-uniform thermal conductivity, Int. J. Heat. Mass Transf. 53 (1–3) (2010) 390–402.
[27] A. Zebib, G.M. Homsy, E. Meiburg, High Marangoni number convection in a square cavity, Phys. Fluids 28 (1985) 3467.
[28] H. Ben Hadid, B. Roux, Thermocapillary convection in long horizontal layers of low-prandtl-number melts subject to a horizontal temperature gradient, J. Fluid Mech. 221 (1990) 77–103.
[29] J.F. Mercier, C. Normand, Buoyant-thermocapillary instabilities of differentially heated liquid layers, Phys. Fluids 8 (1996) 1433–1445.
[30] L. Peng, Y.R. Li, W.Y. Shi, N. Imaishi, Three-dimensional thermocapillary–buoyancy flow of silicone oil in a differentially heated annular pool, Int. J. Heat. Mass Transf. 50 (5) (2007) 872–880.
[31] J. Xu, A. Zebib, Oscillatory two-and three-dimensional thermocapillary convection, J. Fluid Mech. 364 (1) (1998) 187–209.
[32] I. Ueno, T. Kurosawa, H. Kawamura, Thermocapillary convection in thin liquid layer with temperature gradient inclined to free surface, Heat. Transf. 2 (2002) 129–134.
[33] A.I. Mizev, D. Schwabe, Convective instabilities in liquid layers with free upper surface under the action of an inclined temperature gradient, Phys. Fluids 21 (2009) 112102.
[34] P. Cerisier, C. Jamond, J. Pantaloni, J.C. Charmet, Déformation de la surface libre en convection de Bénard–Marangoni, J. Phys. 45 (3) (1984) 405–411.
[35] M. El-Gamma, J.M. Floryan, Thermocapillary effects in systems with variable liquid mass exposed to concentrated heating, FDMP Fluid Dyn. Mater. Process. 2 (1) (2006) 17–26.
[36] T. Bjøntegaard, E.M. Rønquist, Simulation of three-dimensional Bénard-Marangoni flows including deformed surfaces, Commun. Comput. Phys. 5 (2–4) (2009) 273–295.
[37] L. Bammou, K. El Omari, S. Blancher, Y. Le Guer, B. Benhamou, T. Mediouni, A numerical study of the longitudinal thermoconvective rolls in a mixed convection flow in a horizontal channel with a free surface, Int. J. Heat. Fluid Flow. 42 (2013) 265–277.
[38] K. El Omari, T. Kousksou, Y. Le Guer, Impact of shape of container on natural convection and melting inside enclosures used for passive cooling of electronic devices, Appl. Therm. Eng. 31 (2011) 3022–3035.
[39] K. El Omari, Y. Le Guer, Alternate rotating walls for thermal chaotic mixing, Int. J. Heat. Mass Transf. 53 (1–3) (2010) 123–134.
[40] K. El Omari, Y. Le Guer, A numerical study of thermal chaotic mixing in a two rod rotating mixer, Comput. Therm. Sci. 1 (2009) 55–73.
[41] K. El Omari, Y. Le Guer, Thermal chaotic mixing of power-law fluids in a mixer with alternately rotating walls, J. Newt. Fluid Mech. 165 (11–12) (2010) 641–651.
[42] J.R.A. Pearson, On convection cells induced by surface tension, J. Fluid Mech. 4 (05) (1958) 489–500.
[43] R. Touihri, A. El Gallaf, D. Henry, H.B. Hadid, Instabilities in a cylindrical cavity heated from below with a free surface. I. Effect of Biot and Marangoni numbers, Phys. Rev. E 84 (5) (2011) 056302.
[44] S. Chandrasekhar, Hydrodynamic and Hydromagnetic Stability, vol. 2, Oxford University Press, 1961.
[45] D. Johnson, R. Narayanan, A tutorial on the Rayleigh–Marangoni–Bénard problem with multiple layers and side wall effects, Chaos Interdiscip. J. Nonlinear Sci. 9 (1) (1999) 124–140.
[46] E.L. Koschmieder, On convection under an air surface, J. Fluid Mech. 30 (1) (1967) 9–15.
[47] V. Croquette, M. Mory, F. Schosseler, Rayleigh-Bénard convective structures in a cylindrical container, J. Phys. 44 (3) (1983) 293–301.
[48] A.B. Ezersky, A. Garcimartin, J. Burguete, H.L. Mancini, C. Perez-Garcia, Hydrothermal waves in Marangoni convection in a cylindrical container, Phys. Rev. E 47 (2) (1993) 1126–1131.
[49] S. Mergui, X. Nicolas, S. Hirata, Sidewall and thermal boundary condition effects on the evolution of longitudinal rolls in Rayleigh-Bénard-Poiseuille convection, Phys. Fluids 23 (8) (2011) 084101.